Marine snow morphology drives sinking and attenuation in the ocean interior

List of Authors:

Yawouvi Dodji Soviadan[1,9,10*] ORCID 0000-0003-0622-5772

Miriam Beck[1] ORCID 0000-0001-8179-3820

Joelle Habib[1] ORCID 0000-0001-9604-7927

Alberto Baudena[1] ORCID 0000-0002-8890-4324

Laetitia Drago[1, 2] ORCID 0000-0002-0054-1734

Alexandre Accardo[1] ORCID 0009-0008-9426-2250

Remi Laxenaire[3,8] ORCID 0000-0001-5157-1821

Sabrina Speich[4] ORCID 0000-0002-5452-8287

Peter Brandt[5,6] ORCID 0000-0002-9235-955X

Rainer Kiko[1,5,6] ORCID 0000-0002-7851-9107

Stemmann Lars[1,7*] ORCID 0000-0001-8935-4531

1 Sorbonne Université, CNRS, Laboratoire d'Océanographie de Villefranche, UMR 7093 LOV, Villefranche-sur-Mer, France

2 Sorbonne Université, UMR 7159 CNRS-IRD-MNHN, LOCEAN-IPSL, Paris, France

3 Laboratoire de l'Atmosphère et des Cyclones, LACy, UMR 8105, CNRS, Université de La Réunion, Météo-France, Saint-Denis de La Réunion, France

4 Laboratoire de Météorologie Dynamique - IPSL, ENS - PSL, Paris, France

5 GEOMAR Helmholtz Centre for Ocean Research Kiel, Kiel, Germany

6 Faculty of Mathematics and Natural Sciences, Kiel University, Kiel, Germany

7 Institut Universitaire de France, France

8 Center for Ocean-Atmospheric Prediction Studies, Florida State University, Tallahassee, FL, USA

9 Université de Lomé (TOGO)

10 MARBEC, IRD, IFREMER, CNRS, Université de Montpellier, 87 Avenue Jean Monnet, 34200 Sète, France

* Corresponding authors: Yawouvi Dodji SOVIADAN (syawouvi@yahoo.fr or yawouvi_dodji.soviadan@ird.fr) and Lars STEMMANN (lars.stemmann@imev-mer.fr)

Abstract

Simultaneous measurements of marine snow (particles larger than 600 µm) morphologies, estimates of their *in situ* sinking speeds and midwater attenuation in export plumes were performed for the first time using a BGC-Argo float equipped with optical and imaging sensors. The float was deployed and recovered after one year drifting in the sluggish flow regime of the Angola basin. Six consecutive chlorophyll-a and particulate matter accumulation events were recorded at the surface, each followed by an export plume of sinking aggregates. Objects larger than 600 µm were classified using machine learning recognition and clustered into four morphological categories of marine aggregates. Plankton images were validated by an expert in a few broad categories. Results show that different types of aggregates were produced and exported from the different blooms. The different morphological categories of marine snow had different sinking speeds and attenuation for similar size indicating the effect of morphology on sinking speed. However, the typical size-to-sinking relationship for two of the categories and over the larger observed size range (100 µm-few mm) was also observed, indicating the importance of size for sinking. Surprisingly, calculated *in situ* sinking speeds were constantly in the lower range of known values usually assessed *ex situ*, suggesting a methodological effect which is discussed. Moving away from purely size-based velocity relationships and incorporating these additional morphological aggregates properties will help to improve mechanistic understanding of particle sinking and provide more accurate flux estimates. When used from autonomous platforms at high frequency, they will also provide increased spatio-temporal resolution for the observation of intermittent export events naturally occurring or induced by human activities.

1 Introduction

Production, transfer to depth, and remineralization of organic particles provide a major pathway for the export of carbon from the ocean's surface to the ocean interior (Volk and Hoffert, 1985). Phytoplankton photosynthesis and zooplankton trophic activities produce, in the sunlit ocean, particulate matter at the basis of marine food webs. Among the different physical and biological processes determining the fate of the production, gravitational sinking is responsible for 90% of the carbon vertical flux (Boyd et al. 2019). The mesopelagic, here taken as the 100-1000 m layer, is also the starting depth for a myriad of processes such as particle fragmentation, packaging and/or respiration by the mesopelagic fauna that impact (mostly reduce) the flux as particle sink (Burd et al., 2010; Giering et al., 2014; Stemmann et al., 2004). The faster the sinking is, the more carbon is carried to a depth where it can be stored for a long time (Boyd et al., 2019; Siegel et al., 2023).

In the common paradigm, large (>few 100's µm in size) marine particles were thought to be the main vector of the carbon flux (Alldredge and Silver, 1988; Honjo et al., 1982; Stemmann et al., 2002). However, more recently, other particles' characteristics than size (*e.g.*, porosity, ballasting, geometry) were assessed to be important in setting the flux (Cael et al., 2021; Iversen and Lampitt, 2020; Stemmann and Boss, 2012; Williams and Giering, 2022). Particles are often found in the form of aggregates composed of various lithogenic or biogenic elements (Alldredge and Silver, 1988) and their sinking speed depends on the morphological properties of the individual aggregates (size, density, geometry) which depends on the nature of the producers and the aggregation/disaggregation processes (Alldredge and Gotschalk, 1988; Alldredge and Silver, 1988; Iversen and Lampitt, 2020; Ploug et al., 2008a). The efficiency of the deep carbon sequestration depends not only on the aggregates sinking speed but also their attenuation by various mesopelagic processes as they penetrate in the twilight zone of the ocean. A strong vertical flux attenuation in the mesopelagic is usually observed as a result of respiration and particle fragmentation by organisms (Burd et al., 2010; Giering et al., 2014; Stemmann et al., 2004). On one hand, export of fast sinking particles may be less attenuated than slow-sinking ones as they spend less time in this layer but on the other hand, they may be more prone to flux feeding by gatekeeper zooplankton at the base of the mixed layer (Jackson and Checkley, 2011). However, this remains an open question as sinking speed is not only dependent on size (Iversen and Lampitt, 2020) but varies with ballasting (Ploug et al., 2008b, a) and aggregates morphology (Trudnowska et al., 2021) which are barely known.

Because the size of particles is easy to measure *in situ* with imaging systems (Gorsky et al., 2000; Picheral et al., 2010, 2022; Stemmann and Boss, 2012) or *ex situ* in experimental design after production or collection (Iversen et al., 2010; Ploug et al., 2010), the majority of previous studies have calculated sinking speeds, from observations or in models, using a power law relationship between sinking and size (Burd, 2023; Forest et al.,

97 2013; Guidi et al., 2008; Iversen et al., 2010; Kiko et al., 2020; Kriest and Evans, 2000; Soviadan et al., 2022;
98 Stemmann et al., 2004). However, the parameters of this size to sinking relationship vary widely as a function of
99 plankton community composition and aggregation processes (Cael et al., 2021; Forest et al., 2013; Laurenceau-
100 Cornec et al., 2015; Stemmann et al., 2004; Williams and Giering, 2022). In some cases, the relationship was not
101 observed (Diercks and Asper, 1997; Iversen and Lampitt, 2020) or showed an opposite pattern (McDonnell and
102 Buesseler, 2010) questioning the nature of the relationship between size and sinking speed or possible bias due to
103 the experimental methods (Williams and Giering, 2022).

104   Sinking speeds have been generally estimated for decades experimentally, *ex situ,* on collected (or
105 produced) material in 81% of the cases, *in situ* in specific chambers in 14% of the cases and *in situ* by divers in
106 5% of the cases (Cael et al., 2021; Williams and Giering, 2022). More recently, sinking speeds have been
107 calculated by analyzing *in situ* time series of the export plume using optical or camera systems (Briggs et al.,
108 2020; Giering et al., 2020; Stemmann et al., 2002; Trudnowska et al., 2021). There is a debate about whether *in
109 situ* or *ex situ* provides accurate estimates of sinking speed because *in situ* ones tend to be lower (Williams and
110 Giering, 2022). Potential bias in *ex situ* experimental design exists due to physical alteration during collection or
111 production, or because the selected particles for experiments do not represent *in situ* particle assemblages
112 (Williams and Giering, 2022). Conversely *in situ* methods provide an estimate of the bulk particle assemblage,
113 possibly sorted as a function of size. The latest advancement in optical and imaging sensor technology have
114 enabled their integration onto autonomous floats (Accardo et al., 2024; Briggs et al., 2020; Lacour et al., 2024;
115 Picheral et al., 2022). Additionally, recent progress in unsupervised image classification now facilitates the
116 classification of individual aggregates into categories (Accardo et al., 2024; Irisson et al., 2022; Trudnowska et
117 al., 2021). When applied to the study of phytoplankton bloom in the Arctic Ocean, the image classification of the
118 different types of detritus obtained using the Underwater Vision Profiler 5 deployed from a ship, showed, for the
119 first time, a clear relationship between phytoplankton community structure and aggregates morphology with an
120 impact on the sinking aggregate (Trudnowska et al., 2021). Networks of Biogeochemical (BGC)-Argo floats are
121 now deployed with optical sensors to better estimate and understand processes of carbon flux and attenuation
122 (Accardo et al., 2024; Henson et al., 2024; Lacour et al., 2024). Imaging sensors, by providing more qualitative
123 data, will bring a substantial increase in our knowledge of mesopelagic dynamics and the interplay between
124 particles and plankton at scales varying from local to global (Biard et al., 2016; Drago et al., 2022; Laget et al.,
125 2024; Panaiotis et al., 2023; Stemmann et al., 2002, 2008).

126   In this study, we analyze the results of image analysis of a recovered Underwater Vision Profiler 6
127 (UVP6) camera mounted on a BGC-Argo float from May 2021 to April 2022 drifting in the sluggish flow regime
128 of the Angola basin. During the one-year deployment, the float drifted slowly in a region with weak currents and
129 low mesoscale activity. Seven consecutive marine snow production events were recorded at the surface and six of
130 them lead to an export plume of sinking aggregates. Unsupervised classification of all the marine snow aggregates
131 was performed to identify the different types of particles. The objectives of this work are i) to automatically
132 classify *in situ* images of marine snow, ii) to describe the assemblage of marine snow particles at the surface and
133 in the mesopelagic during the six intermittent production and export events and iii) infer marine snow
134 morphotypes sinking velocities and vertical attenuation in the export plume. To our knowledge, this work provides
135 the first estimates of sinking speeds and export attenuation for different types of particulate materials recorded
136 from a BGC-Argo float.

2 Methods

2.1 BGC-Argo float deployment
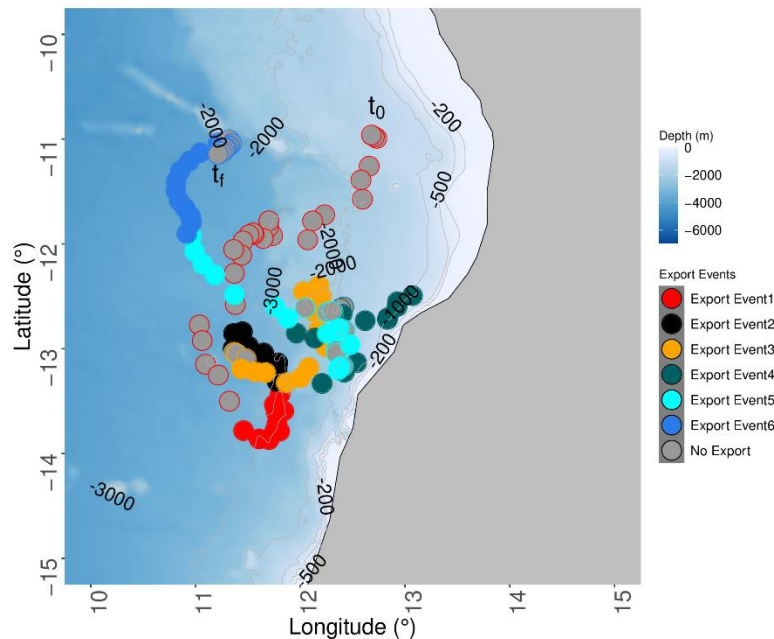
Figure 1: Angola region of the BGC-Argo float deployment with the trajectory during the one-year drift. The filled dots correspond to the 6 export events and the colors of unfilled dots indicate the period before each export event in the same color except for the last period for which it indicates after the export. The beginning (11° S, 12°45' E noted t_0) of the period before the export event1 indicates the float position at its deployment and the end of (11°10' S, 11°13' E noted t_f) the period after export event6 indicates the position at its recovery.

The BGC Argo float (WMO:6903096) was deployed on 4 May 2021 at 11° S, 12°45' E during RV Sonne cruise SO283 and retrieved on 26 April 2022 at 11°10' S, 11°13' E during RV Meteor cruise M181. Distance between surfacing every three days was on average 16 km +/- 11.73 with 4 periods (May 2021, June 2021, December 2021, February 2022) when the drift could reach 40 km in three days. In general the float was programmed to reach a maximum depth at 1000 m and when possible every 4 profiles to reach 2000 m (Fig. 1). When the bottom depth was shallower than 1000m the float maximum depth was set to be 20 m above seabed. The general pattern of the drifting was toward south, almost reaching 14° S in August 2021, then north-eastward toward the isobath 700m depth which was reached in early December 2021. Thereafter, the float drifted toward south-west along the isobath 700m until the end of December 2021. The float drifted away from the coast toward north up to the latitude 11° N at which it was recovered.

2.2 Environmental and satellite data

2.2.1 Float data (CTD, Chla, Bbp POC)

The float was equipped with several sensors to characterize the properties of the water column. First, to measure hydrological parameters, the float was fitted with pressure (DRUCK_2900PSIA), temperature, and salinity sensors (SBE41CP_V7.2.5). Second, to measure biogeochemical properties, it was equipped with oxygen (AANDERAA_OPTODE_4330), fluorescence (proxy for Chla) and backscattering (700 nm, referred as Bbp POC taken as a proxy for all suspended particles ap.<10 µm) sensors (ECO_FLBB_2K). Fluorescence and backscatter were converted to units of Chla (mg m^{-3}) and particulate organic carbon (POC, mgC m^{-3}) as in Accardo et al. (2024). The UVP6 was mounted on the float. All data (CTD, optical and UVP6 particle size distribution) were recorded during the ascent of the float, and are made freely available by the International Argo Program http://doi.org/10.17882/42182#117069 (float with WMO 6903096, link accessible on 25/03/2025). We did not

167 apply additional quality control (QC) procedures beyond those already implemented in the standard Argo QC
168 protocols and derived data were calculated as in Accardo et al., (2024).

2.2.2 Satellite data (SSH, Lagrangian diagnostic)

170 Several Lagrangian diagnostics were computed at each profile location using velocity data and
171 environmental satellite products. Firstly, for each station (*i.e.*, profile location) a region considered as
172 representative of the water column sampled by the float was defined. This region, in this study, was a circular
173 neighborhood of radius r of 0.1° around each exact profile location. Then, this circular shape was filled with virtual
174 particles at the surface separated by 0.01° (resulting in ~300 particles). Afterward, the next step was to compute
175 for each virtual particle several Lagrangian diagnostics. This led to about 300 values for each sampling station
176 which were averaged together, providing a given diagnostic around each profile location. The choice of using a
177 circle around the float profiling location is done to smooth the errors associated with the velocity field uncertainty,
178 as shown in previous studies (Baudena et al., 2021; Chambault et al., 2019; Ser-Giacomi et al., 2021). The velocity
179 field used was derived from both altimetry and assimilation model delayed-time data and includes the geostrophic
180 and the Ekman components (Copernicus Marine Environment Monitoring Service (CMEMS) product
181 MULTIOBS GLO PHY REP 015 004-TDS). It was used to advect each virtual particle (within the representative
182 water parcel) from the profile day until an advective time (τ) ranging between 5 and 45 days backward in time.
183 For each advective time, a diagnostic mean value was available for each profile. Diagnostics were numerous, so
184 only those which provided significant results will be developed here. The first one used was the Finite-Time
185 Lyapunov Exponents (FTLE, days^{-1}). This metric is useful to identify frontal features (Baudena et al., 2021). In
186 this study, a front is defined as a physical barrier at the surface that separates two water volumes of different
187 hydrographic properties that likely were very far from each other in the previous days. FTLEs were calculated as
188 in (Shadden et al., 2005) and the main parameter that was considered was the initial separation between two virtual
189 particles. The second diagnostic used was the Lagrangian chlorophyll-a (mg m^{-3}), *i.e.*, the mean chlorophyll
190 content along the backward particle trajectory. These metric estimations were computed thanks to satellite data of
191 surface chlorophyll-a concentrations which was provided by CMEMS Copernicus website (delayed-time satellite
192 product "OCEANCOLOUR GLO BGC L4 MY 009 104-TDS").

2.3 Particle data taken by UVP6

2.3.1 A broad size classification of all particles into two size categories

195 A broad size classification was applied on raw size particles spectra data (>100 μm up to few mm)
196 provided by the UVP6 (without any plankton identification). In this case the assumption was made that
197 zooplankton represent only a small fraction of objects sampled by the UVP6 compared to particles. Then, size
198 range was divided into two sub-classes: MiP (Micrometric Particles) integrating the concentrations over all size
199 classes between 0.1 and 0.5 mm and MaP (Macroscopic Particles) integrating the concentrations of size classes
200 between 0.5 and 16 mm. This lower threshold was used because it corresponds to the definition of marine snow
201 (Alldredge and Silver, 1988). The vertical flux of these two categories was calculated assuming an empirical
202 relationship to convert particle size to POC and another one to obtain sinking speed from size (Kriest, 2002) (with
203 reference 2a of Table 1 and reference 9 of Table 2 for mass and sinking speed of a particle) and previously used
204 in the inter tropical Atlantic Ocean (Kiko et al., 2017, 2020).

2.3.2 Unsupervised morphological classification of marine snow in four categories

206 All images were retrieved from the Ecotaxa web site (https://ecotaxa.obs-vlfr.fr/gui/prj/7608, link
207 accessible on 25/03/2025). An unsupervised classification method was applied, following an approach previously
208 used to study marine snow in the Arctic Ocean (Trudnowska et al., 2021) and in the Southern Ocean (Accardo et
209 al., 2024).
210 Prior to the analysis, zooplankton and particle images were separated by supervised classification and
211 treated independently. The first step consists in summarizing the 27 morphological features that were derived
212 from the individual particle images. Those features (Table S1) describe their size (e.g., area, perimeter), shade

213 intensity (e.g., mean/median gray level), shape (e.g., symmetry, elongation), and structure (e.g., homogeneity or
214 heterogeneity, mostly based on the variability in gray level). To reach a normal distribution of each variable,
215 extreme values (below or above the 5th and 95th percentile) were flagged as NA - which is interpreted neutral by
216 the following methods - before applying the Yeo-Johnson transformation (Yeo and Johnson, 2000). These traits
217 were then summarized via dimensionality reduction using Principal Component Analysis (PCA). The PCA
218 function scales the features to unit variance prior to the analysis and creates a multi-dimensional "morphospace"
219 in which each particle was positioned based on its morphological features. As in the work of (Trudnowska et al.,
220 2021), size turned out to be the main morphological trait. Therefore, we repeated the same procedure by removing
221 all size-related features (-area, -perim., -major, -feret, -convperim, -skeleton_area, -convarea_area, -
222 symetrieh_area, -symetriev_area, -elongation) to hopefully better distinguish the particles by their other
223 morphological traits. To assess the sensitivity of this classification we also tested alternative algorithms within
224 this approach (see section Sensitivity of aggregates classification to the method in Supp. Mat.). In particular, we
225 tested UMAP (McInnes et al., 2018), a method of dimensional reduction to define the morphospace. In contrast
226 to PCA which creates a linear projection, UMAP is a non-linear dimensional reduction method that has been used
227 previously in similar contexts (Stolarek et al., 2022; Teixeira et al., 2022). To ensure comparability with the PCA,
228 data was scaled prior to the application and four axes were retained to define the morphospace. All other
229 parameters were kept with the same default values (n_neighbors=15, min_dist=0.1) since the resulting
230 morphospace separated the particles as expected.

231 The second step, the classification, was the same for all options (PCA/ UMAP, with/ without size-related
232 features). A k-means clustering was performed on the particles' coordinates on the first four principal components
233 of a morphospace. The number of clusters ("k") was set to four, a value which in several simulations conducted
234 the best trade-off between partitioning into visually clearly distinct groups of particle morphology and simplicity
235 in the following analysis. See section Marine snow classification in Supp. Mat. for a test of k=5 and 10 to assess
236 the impact of this choice on the result. Finally, the concentration (nb m^{-3}) of each morphotype was computed by
237 dividing the number of particles found in each depth bin by the volume sampled by the UVP6. To study their
238 spatio-temporal distributions, group concentrations were interpolated according to depth and time with a
239 resolution of 5 meters and one day respectively.

2.4 Data analysis

2.4.1 Sinking speed and particle vertical attenuation

242 We calculated the sinking speed for six export plumes that were detected by successives peaks at different
243 depths (Fig 2). Assuming constant sinking velocity in the upper 1000m and a Lagrangian drift in a weak vertical
244 shear environment during the short marine snow production events (on average <1 month), we followed the
245 published method developed to survey the evolution of export plumes developed for optical and imaging systems
246 (Briggs et al., 2020; Lacour et al., 2024), In this vertical binning approach more appropriate for large particles, a
247 Gaussian fit is applied to the median concentration of different aggregate size classes per 100 m depth bins. For
248 each size class and type of marine snow, a linear regression was done on the coordinates in depth and time of each
249 of the Gaussian fits' maximums. The value of the slope and the concentrations of the particles at the different
250 depths were stored if the Gaussian fit was successful for at least 3 depth layers. The slope is an indicator of the
251 sinking speed, while the particle vertical gradients were modeled using a power law model ($N(z)=N_{100}.(z/100)^{-b}$)
252 with a reference depth at 100 m to retrieve the b exponent as an indicator of particle attenuation. This method was
253 initially proposed for POC flux measured in sediment traps (Martin et al., 1987) and vertical flux obtained with
254 profiling cameras(Guidi et al., 2008, 2015), but here it was applied to aggregate concentrations in export plumes
255 as in (Trudnowska et al., 2021). Due to the non-sinking behavior or because of the low signal-to-noise ratio in the
256 upper size range where particles are rare, this approach did not work for all size classes in all categories.

257 Finally, sinking speeds as a function of size and aggregate types were also calculated over the whole
258 deployment with lagged correlation between time series in two different depth layers (0-100 and 300-400 m). The
259 lag with the maximum correlation indicates the time for the different particle communities to sink from the upper
260 layer to the deeper layer (average distance of 300 m).

2.4.2 Canonical Redundancy Analysis (RDA) of particle assemblage

For each depth layer, a canonical redundancy analysis (RDA) was performed based on the abundances of the 4 marine snow morphotypes and the above-mentioned environmental variables to explore the explanatory power of these variables in structuring marine snow. The RDA is an extension of the multiple regression analysis applied to multivariate data (Legendre and Legendre, 2012). It allows representing the response variables (abundances of the 4 categories) in a "constrained" reduced space, i.e., constructed from the explanatory variables (the environmental variables). For each RDA, the following variables were used as "supplementary variables" of the analysis to visualize their correlation with the environmental structuring of marine snow assemblage (i.e., to visualize their position in the RDA space). Beforehand, a Hellinger transformation was performed on the abundances in order to reduce the impact of large concentration values. Significant axes were identified using the Kaiser-Guttman criterion (Legendre and Legendre, 1998).

2.4.3 Identification of intermittent production and export events in a marine snow time series

We determined the marine snow production and export events using their time series in 5 depth layers (Fig. 2). Major peaks were found in the different layers at a few months intervals. Except for the first surface peak (0-100 m) in May 2021, the subsequent six surface particle peaks were followed by peaks in the mesopelagic layer (noted 1 to 6 in Fig. 2). The beginning of each period was set at the start of marine snow accumulation in the first layer and the end was set at the time of the subsequent minimum in the deeper layers. Throughout the manuscript, we will refer to these six events as "plumes" or "events". Apart from these 6 main peaks, we observed between period 2 and 3 and between period 4 and 5, two small peaks in surface concentrations that translated into weak peaks in the deeper layer for the first one. Converted to biovolume (Fig. S8), these small events were more visible suggesting that they were composed of mainly large rare particles. They were not included in further analysis because they did not meet the quality control to estimate sinking speeds (see section 2.4.1) due to the more noisy time series of rare large objects.
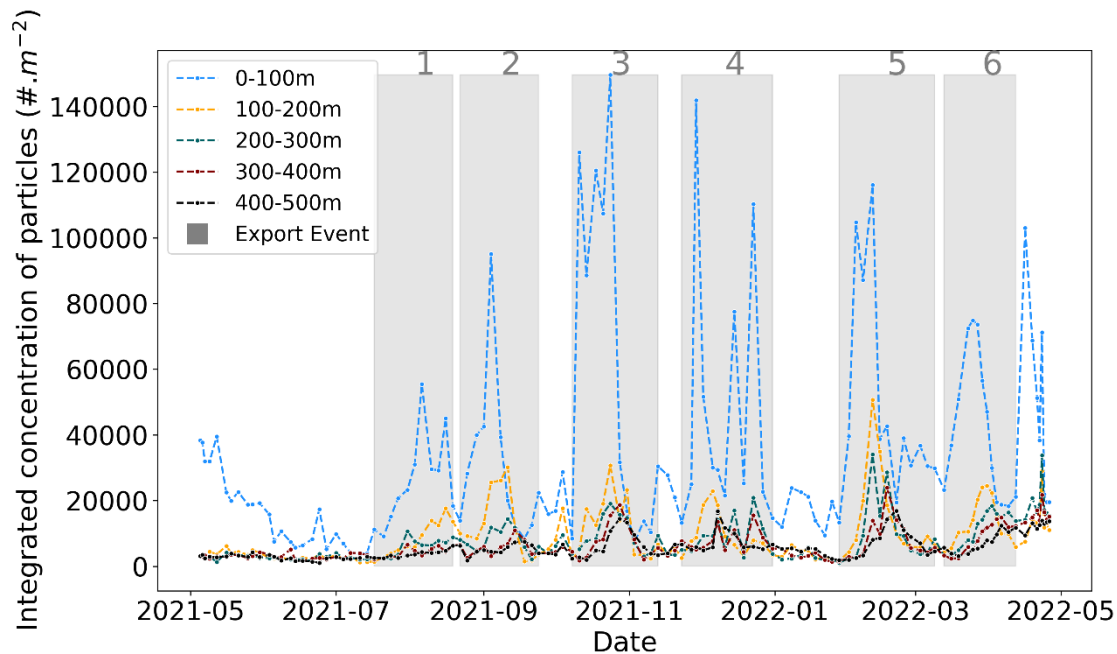
Figure 2: Time series of vertically integrated marine snow (MaP, all particles >600μm) concentrations (# m⁻²) in 5 layers in the upper 1000 m depth. The 6 bloom periods shaded in gray correspond to six export events that are marked by delayed peaks in the mesopelagic. The periods are defined for the events in 2021 as 07/17-08/19, 08/22-09/24, 08/10-11/13, 11/23-12/31 and in 2022 as 01/28-03/09 and 03/13 to 04/12.

3 Results

3.1 Epipelagic time series of hydrological and biogeochemical properties
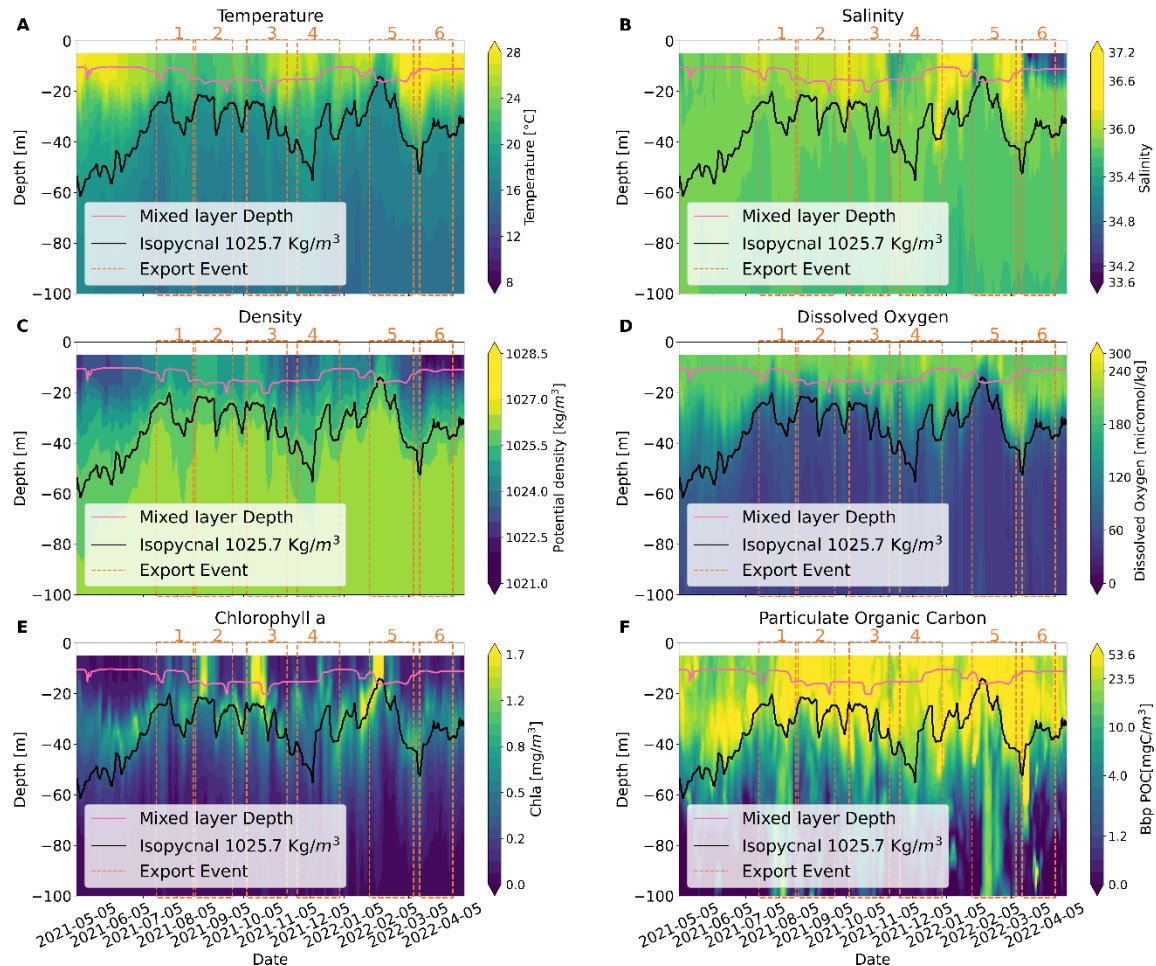
Figure 3: 0-100 m, 2D time series of A) temperature, B) salinity, C) density, D) dissolved oxygen, E) chlorophyll *a* concentration and F) Bbp POC. The black line depicts the 1025.7 kg m^{-3} isopycnal. The red line represents the mixed layer depth.

Sea surface temperature showed the lowest temperatures (21-23°C) from July to September 2021, with the highest temperatures recorded in March and April 2021 (up to 28°C) (Fig. 3). Sea surface salinity exhibited low values in November 2021 (<35) and particularly from March to April 2022 (<34.2). Densities within the upper 30 m depth showed their lowest values from May to June, from mid-October to December 2022, and after February 2022. The isopycnal 1025.7 kg m^{-3} used as an indicator of upwelling (Körner et al., 2024), was shallow (20-30m) between July and October 2021, and as well as from December 2021 to mid-February 2022. It reached its maximum depth in May-June, December 2021 and early March 2022. Highest Chl*a* concentrations were always found in the upper 30 m with an important deep chlorophyll maximum (DCM) around 30-40 m depth. The DCM oscillated within this depth range following the rise of the 1025.7 kg m^{-3} isopycnal, displaying periods of intensification along with an upward movement towards the surface (notably in August, October 2021, and February 2022 concomitantly to the export periods 2, 3 and 5). From May to July 2021, the peak of small particles or Bbp POC followed the DCM but thereafter to the end of the deployment (May 2022) extended from the surface down to the isopycnal 1025.7 kg m^{-3}. During three periods of strong export (periods 1, 3 and 5), elevated Bbp POC (>3 mgC m^{-3}) were observed extending down to a depth of 100 m.

310 **3.2 Full Depth (0-1000m) time series of Bbp POC, MiP and MaP**
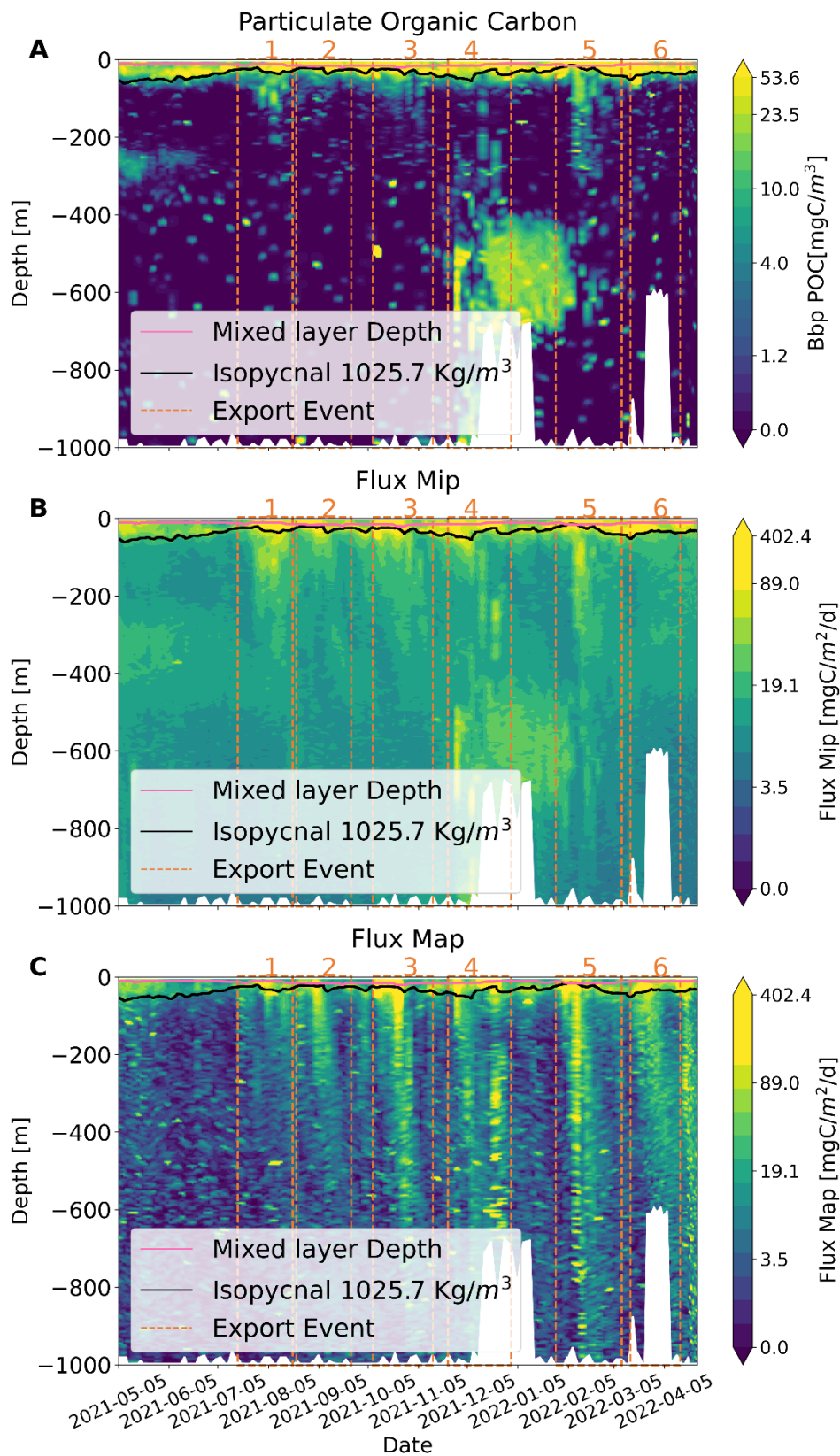
311
312 **Figure 4: Time–depth profiles determined from the BGC Argo float for A) Bbp POC, B) MiP flux, and C) MaP flux**
313 **(in logarithmic scale) as a function of time and depth with the 6 export periods being illustrated by the red vertical**
314 **dashed lines. The black line depicts the 1025.7 kg m⁻³ isopycnal. The maximum depth of the float corresponds to the**
315 **bottom depth, marked by a white mask. The red line represents the mixed layer depth.**

316   Small particles detected by the Bbp sensor (few µm) and the MiP (0.1<ESD<0.5mm) flux detected by
317 the UVP6 showed remarkably similar temporal patterns with different vertical extensions notably during the
318 export events. They showed all along the deployment highest values in the upper 100 m depth (Fig. 4 a-b). A
319 distinct midwater peak was observed from May to June 2021 between 250 and 300 m depth for Bbp POC and
320 from 300 to 400 m for MiP. Very high Bbp POC (>20mgC m-3) and MiP (>20mg C m-2 d-1) were observed from
321 400 to 600 m depth at the time when the float was in a shallow region in December 2021. Apart from this deep
322 occurrence, the Bbp POC vertical extent reached 250 m at maximum during periods 1, 3 and 5. The MiP penetrated
323 deeper in the water column down to 300 m depth during all export periods (albeit more in periods 1, 2, 3 and 5,
324 August, October and December 2021, February 2022 respectively).
325   In contrast, large particles as indicated by the MaP (>500 µm) flux showed a distinct spatio-temporal
326 pattern, with the highest values occurring in the upper 100 m depth (100-400 mgC m^{-2} d^{-1}) differently from the
327 Bbp POC and Mip which showed maximum concentration in midwater layers. Following July 2021, the MaP flux
328 exhibited 6 intermittent events (>100 mgC mgC m^{-2} d^{-1} Fig. 4c), during which export plumes showed oblique
329 patterns extending from the surface down to the mesopelagic particularly in August (period 1), September (period
330 2), October (period 3) and December (period 4) 2021 and February (period 5) and April (period 6) 2022. These
331 occurrences, notably in October 2021 and February 2022, reached depths down to 1000 m, leading to a two-fold
332 increase in the computed flux during the export relative to the situation before and after.

333 **3.3 Image classification of marine snow >600 µm into four morphotypes**
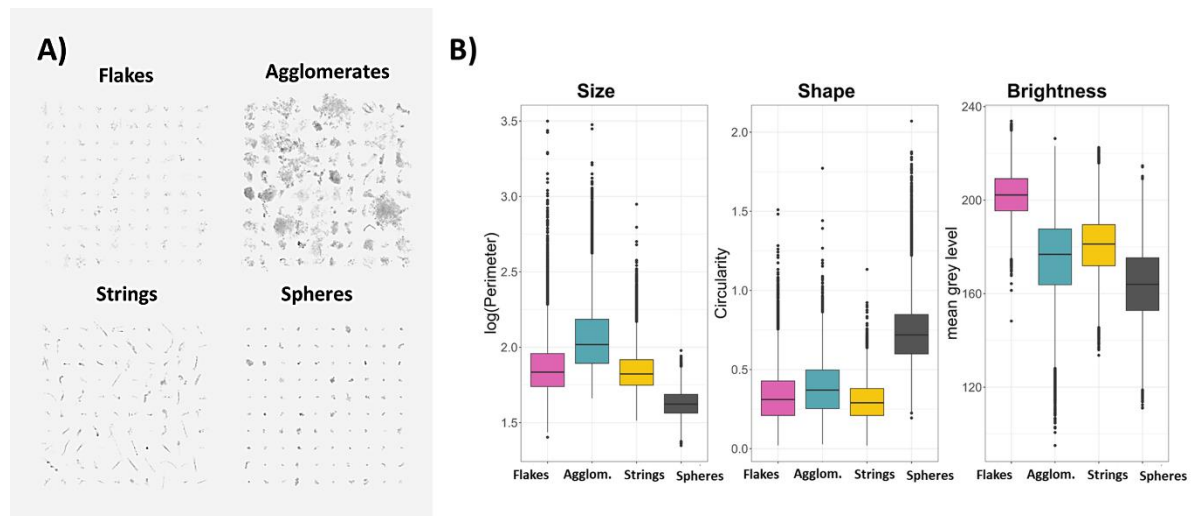
334
335 **Figure 5: A) Example vignettes of the four defined morphotypes (flakes, agglomerates, strings and spheres) , we applied**
336 **microsoft windows photo software changes to the vignettes with contrast (-40%), brightness (-8%), sharpness (100%)**
337 **and B) their mean morphological traits describing main aspects of size (via perimeter (µm)), shape (via circularity,**
338 **dimensionless) and brightness (via mean gray level, dimensionless range 0 black to 256 white pixel).**
339
340   To depict the nature of the sinking aggregates, we classified them performing k-means clustering on the
341 coordinates of particles along the four retained PCA axes. Within this continuous morphospace, we identified four
342 morphotypes (Showed in Fig. 5A), selected as a suitable compromise between contrasted groups and contextual
343 knowledge to explain their nature. Cluster 1 corresponds to medium-sized and bright aggregates named **flakes**
344 (mean perimeter = 1.86 µm, mean circularity = 0.33, mean brightness = 202.46, Fig. 5). Cluster 2 contains large
345 and dark particles named **agglomerates** (mean perimeter = 2.06 µm, mean circularity = 0.38, mean brightness =
346 174.91). Cluster 3 contains medium-sized and elongated aggregates named **strings** (mean perimeter = 1.84 µm,
347 mean circularity = 0.30, mean brightness = 180.69). Cluster 4 is composed of small and circular aggregates named
348 **spheres** (mean perimeter = 1.63 µm, mean circularity = 0.73, mean brightness = 163.87). More results on marine
349 snow classification and on the sensitivity of aggregates classification to the method is provided in Supp. Mat.).

3.4 Spatio-temporal distribution of marine snow morphotypes (>600μm)

The different marine snow types showed concentrations of similar magnitudes varying from 0 to 20 000 particles m^{-3}. Surface concentrations were two to three fold higher than in the mesopelagic. From May to July 2021, all particle types showed reduced concentrations (in particular in the mesopelagic) compared to the rest of the period which showed an intermittent pattern (Fig. 6). The different particle types shared similar overall spatio-temporal dynamics mainly in the surface but also exhibited distinct features in the deep. In the surface layer and the upper mesopelagic (200-400 m), they all showed concomitant peaks during the bloom periods. In the deeper mesopelagic only agglomerates and spheres showed an increase with a time delay increasing with depth.
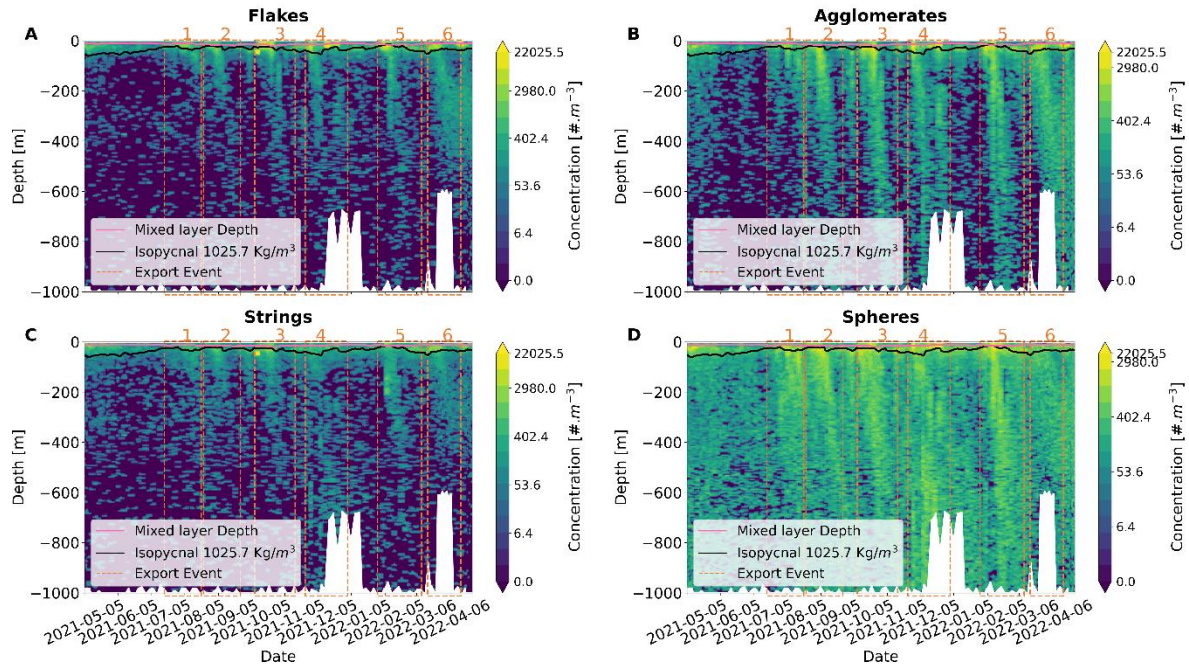
Figure 6: Contour plot of the four marine snow types: A) Flakes, B) Agglomerate, C) Strings, D) Spheres, as a function of time and depth. The 6 export events are depicted by the red vertical dash lines. The black line depicts the 1025.7 kg m^{-3} isopycnal. The maximum depth of the float corresponds to the bottom depth, marked by a white mask.

3.5 Spatio-temporal dynamics of marine snow assemblage

As illustrated in the RDA composite spaces, marine snow assemblages in the surface layer varied with seasons and also between surface and mesopelagic layer (Fig. 7). In the surface layer, contributions to axis 1, reveal the opposite dynamics between spheres and strings compared to flakes and agglomerates. Strings dominate from May to July (before export event 1), spheres from May to October (from export event 1 to export event 3), and agglomerates after February (after export event 5). The first two export events had consistent and homogeneous assemblages dominated by spheres. Subsequent export periods (3, 4, and 5) exhibited varying assemblages, mainly dominated by strings and spheres. The last period (after February) that includes export event 6 differed greatly in the assemblage with a dominance of agglomerates. When comparing periods before and during an export event in the surface layer, apart from the first event, the assemblage did not change. In the deeper layer, the assemblage composition evolution was consistent with the surface one but was more contrasted with less balanced assemblages as indicated by the higher contribution of the first axis (86.9%) relative to the surface (51.6%) (Fig. 7). In the mesopelagic, contributions to this axis reveal the opposite dynamics between spheres compared to flakes and agglomerates. Apart from export event 6, all export events were dominated by spheres. Noticeable is also a more pronounced difference between export events 2 (higher proportion of strings) and 3 (higher proportions of agglomerates and spheres) relative to the surface evolution. Dominance of flakes was not observed.
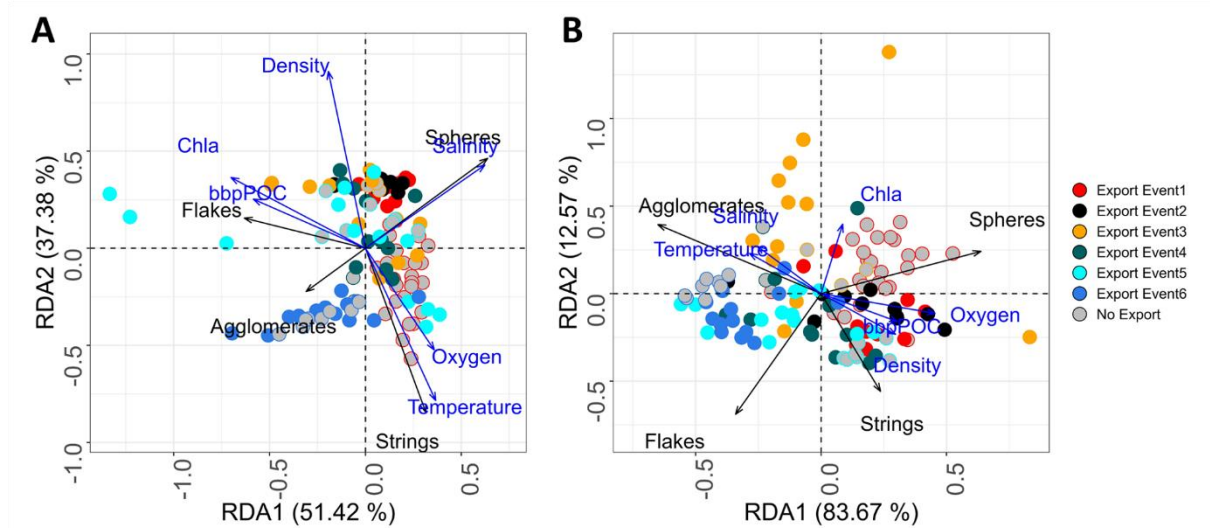
380
381 **Figure 7: RDA of marine snow assemblages at each station (dots) A) between 0-100 m (left panel) and B) 400-500 m**
382 **depth identifying the six periods of export with different colors. Stations observed prior (in gray) to the export event**
383 **are encircled according to the color of the event. Black arrows show the dominant type of marine snow while the blue**
384 **arrows show the correlation with environmental variables.**

385 **3.6 Sinking speed and vertical attenuation of the plume**

386   Sinking speeds, inferred from the lagged correlation between surface and mesopelagic (400-500m)
387 particle time series, for all types of particles (MiP, MaP, morphotypes 1 to 4) were of 30 m d^{-1} (Supp. Table S2).
388 By separating the six events and with more size related classification, more details can be obtained to break apart
389 this constant estimate. However, sinking speeds and attenuation in a plume can only be determined for a given
390 size range if the abundance variability in the time series is consistent. This was not the case for each size class and
391 category among the 60 possibles cases (6 plumes*10 size ranges from 100 µm to 5 mm). Sinking speeds could be
392 estimated 6 times for flakes, 19 times for agglomerates, 5 times for strings and 12 times for spheres. When
393 averaging altogether the results from the six export events, a unique size-based relationship is not visible for the
394 different morphotypes (Fig. 8A), but agglomerates and spheres showed the highest sinking speeds. Also within
395 the size range for which sinking estimates were possible for all morphotypes (ESD from 1.02-1.29 mm), spheres
396 (46+/-24 m d^{-1}) and agglomerates (35+/-9 m d^{-1}) showed higher sinking speeds relative to flakes (16.29±4 m d^{-1})
397 and strings (18.33±6 m d^{-1}) (Table S3). When considering the abundance of all particles >100 µm (MiP+MaP),
398 sinking speed estimates could be performed in 16 cases (mostly for particles larger than 500 µm). Sinking speed
399 increased with size from a minimum of 10 m.d^{-1} to a maximum of 150 m.d^{-1}. It is noticeable that sinking speed
400 estimation for the largest size classes (>1.02 mm) was not possible when considering all particles but possible for
401 agglomerates.
402   The strength of particle abundance attenuation in the plume increased on average with particle size and
403 showed a remarkable difference between the different morphological types. Spheres had the lowest attenuation
404 while flakes and strings had the strongest. For spheres, the attenuation decreased as a function of size. For size
405 class 3 (1.02-1.29 mm), spheres (0.27+/-0.23) and agglomerates (0.88+/-0.3) had the lowest attenuation compared
406 to flakes (1.86+/-0.21) and string (1.76+/-0.1) (see Table S3). Apart from spheres, for which attenuation decreased
407 significantly with size, no relationship between attenuation and size was found. Extending the size range by
408 pooling all particles does not evidence an allometric relationship.
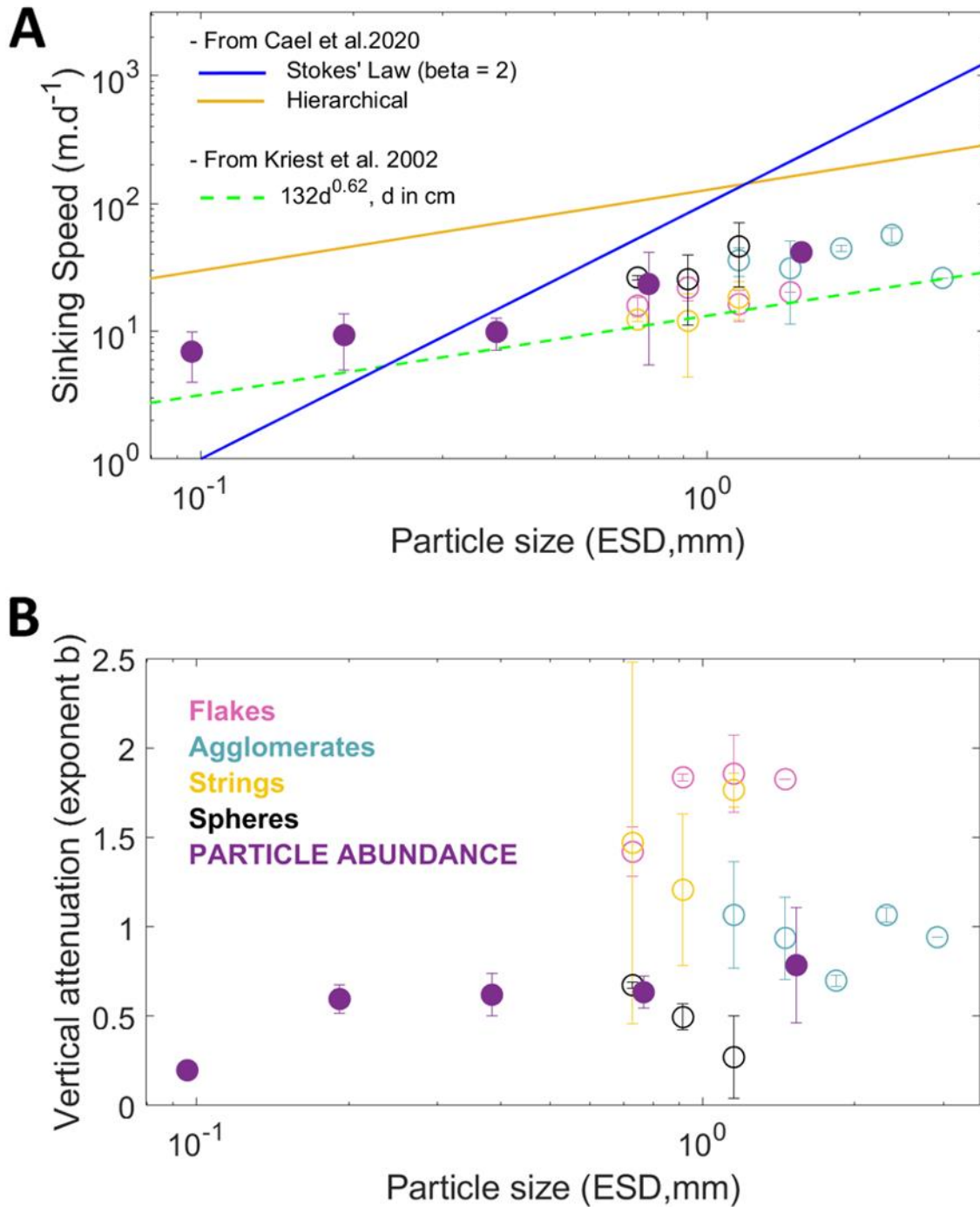
409
410 **Figure 8: Sinking speed versus size (A) and attenuation exponent *b* versus size (B) for different types of particles**
411 **averaged for the six different export events. The solid blue line is the Stokes' Law relationship, valid for spherical**
412 **smooth particles with a constant excess density with increasing size and the orange line is the hierarchical regression**
413 **on the data compilation in Cael et al., 2021. Dashed green line represents the model parametrizations of size-sinking**
414 **relationship by (Kriest, 2002).**
415
416
417

4 Discussion

4.1 Hydrological context and ocean circulation during the drift

The observed hydrographic characteristics are in general agreement with the seasonal variability of the region. Sea surface temperature, primarily driven by surface heat fluxes, showed the lowest values from July to September and the highest values in March and April (Körner et al., 2023; Scannell and McPhaden, 2018). Sea surface salinity as measured by the float was lowest in November and from March to April. The timing of freshening is in agreement with the seasonal advection of low-salinity waters with the southward-flowing Angola Current (Awo et al., 2022; Kopte et al., 2017). While sea surface temperature shows a dominant annual cycle, upwelling and downwelling near the continental slope are characterized by both an annual and semiannual cycle. Consistent with previous study, the main upwelling season happens during the cold period from July to September while the secondary upwelling season occurs during January to February (Körner et al., 2024). During these periods, float data indicate denser water with minimum oxygen concentrations close to the surface. As there is, in general, good anti-correlation between oxygen and nitrate (Körner et al., 2024), it is possible that during upwelling periods low-oxygen and high-nitrate water enters into the euphotic zone, fueling the six observed production/export events identified in the float data. Periods 1 and 2 are within the main upwelling season and period 5 is during the secondary upwelling season. While period 3 might be during the transition from upwelling to downwelling, periods 4 and 6 were clearly during the secondary and main downwelling seasons, respectively. Note that between April and August 2021 an extreme warm event was present in the Angola basin associated with record low productivity between June and August partly covering the main upwelling season (Imbol Koungue et al., 2024).

During the deployment, the float drifted slowly with an average distance between surfacing of 16 km in 3 days. The highest drift (40 km in three days) was observed during periods 3 and 5. ADT shows weak horizontal variability suggesting that the eddy field is present but with low intensity (Fig. 4 in Supp. Mat.). FTLE values generally less than 0.1 d^{-1} indicate weak eddy activity as generally reported in the region (Aguedjou et al., 2019). The negative correlation between all types of particles and FTLE indicates that the bloom events followed by particle accumulation were more intense at low horizontal mixing. The intermittent exports are associated with bloom events that are connected to coastal blooms during periods 4, 5 and to a lesser extent 6. In order to identify the marine snow export plumes (and thus calculate the sinking speeds and vertical attenuation), we made the hypothesis that the water parcel encompassing each plume did not change considerably while the float profiled them. While this Lagrangian assumption cannot be demonstrated with the available data set, different supplementary analyses suggest (Fig. S5, Table S2) that this approximation seems reasonable. The hydrological properties of the mesopelagic, as well as the oxygen concentrations, showed a weak variability during the study period. Low turbulence was observed in the region, as shown by relatively low FTLE values and by the fact that the float did not get trapped in any mesoscale eddy. In addition, previous studies showed a weak vertical shear environment in this region (Kopte et al., 2017). Delayed occurrence in large particle peaks with depth, supports this 1D hypothesis as in previous studies (Briggs et al., 2020; Lacour et al., 2024; Stemmann et al., 2002; Trudnowska et al., 2021) which is not observed in case of strong mesoscale activities (Accardo et al., 2024). A typical mesopelagic nepheloid layer (visible on Bbp POC and MiP), presumably extending from the seafloor was observed as the float was drifting along the 700 m depth bathymetry. This feature was also observed in the MiP but not in the larger particles (Fig. 4C and 5). Such size differentiated distribution across continental shelves has already been observed elsewhere with combined optical and imaging methods (Durrieu de Madron et al., 1990, 2017). This observation suggests that the nepheloid layers did not contain any large aggregates and therefore did not interfere with our sinking estimates for the large fractions (MaP and the 4 morphotypes) but potentially not for the MiP.

4.2 Dynamics of the six marine snow events

The four marine snow morphotypes were correlated to *in situ* or remotely sensed Chl*a* suggesting that most of the marine snow was of phytoplanktonic origin (Supp. Fig. S5). Additional material (*i.e.,* phytoplankton in bottles and zooplankton in net) as available in a previous study (Trudnowska et al., 2021)is needed to unambiguously attribute a morphotype to a specific phytoplankton or zooplankton community. However,

correlation with environmental variables and the shape of particles suggest possible sources of the four types of marine snow. Typical dense fecal pellets, relative to loose marine snow, were not detected by the unsupervised classification but they probably are mostly contained in spheres which contained the most opaque and small particles. Given the observed lower 0-100 m integrated concentration of zooplankton organisms (observed range 10^3-10^4 ind.m^{-2}) relative to marine snow (observed range 10^3- 20 10^4 ind.m^{-2}) as generally found in other studies (Checkley et al., 2008; Forest et al., 2012; Gonzalez-Quiros and Checkley, 2006; Stemmann and Boss, 2012; Trudnowska et al., 2021), it is possible that the contribution of fecal pellets to the total detritus was low. A lower abundance of pellets relative to marine snow was also observed in sediment traps (Durkin et al., 2021) and episodic export of phyto-detritus to the deep is a common feature in many sites (Turner, 2015). The three other categories are probably mostly phytodetritus. It is likely that the two clusters of strings/filaments contained living phytoplankton colonies as they were mostly abundant in the surface water at the time when trichodesmium colonies were detected before the first export event (Supp. Fig. S4). While we acknowledge that the classification in 4 morphotypes may not represent all existing morphological variability, it seems appropriate for our case study. Four to five categories were also useful in other studies (Accardo et al., 2024; Trudnowska et al., 2021). Having four instead of five categories increased the concentration by categories yielding more confidence in estimations of the dynamics of marine snow assemblages, their sinking speeds, and attenuation, while still differentiating the main morphological features of particles. In the future, global compilation of such images together with other phytoplankton and zooplankton variables will allow to refine the number of existing morphotypes.

According to the float and satellite observations, the blooms seem to be triggered by different dynamics. Blooms 1, 2, and 3 seem to be associated with typical open ocean upwelling events, as suggested by decreased temperature and oxygen associated with higher Chl*a* and Bbp POC. Conversely, the three other events (and in particular 4 and 6) were associated with less salty water. Low salinity is possibly an indicator of coastal input from particle enriched water stemming as far off the Congo river (Brandt et al., 2023). The float was closest to the coast and drifted along it (along the isobath 700 m depth) during period 4. During periods 5 and 6, the float drifted offshore and surface Chl*a* showed filaments extending from the coast (Fig. S2), corroborating the hypothesis of coastal inputs. The bloom in period 5 was probably associated with more nutrients as suggested by the rising of the 1025.7 kg m^{-3} isopycnal. The sequence of events leading to marine snow accumulation for periods 4 and 6 is less clear as the isopycnal 1025.7 kg m^{-3} was deep and Chl*a* biomass was not so high. However, overall significant correlations between temperature, oxygen, density, and all biogeochemical variables (Chl*a*, Bbp POC suspended particles, MiP, MaP, and all zooplankton taxa; (Supp. Fig. S5) suggest that upwelled water triggered an increase in the planktonic production.

Apart from the first export event, the different marine snow morphotypes did not change in their relative contribution before and during the export events. The main changes in marine snow assemblages were associated with depth during all events and time (the last event being dominated by agglomerates). The increase with depth of the proportion of spheres is related to a clear reduction in filaments and flakes as previously observed in other systems (Accardo et al., 2024; Trudnowska et al., 2021). These changes suggest that flakes and filaments are less efficiently exported than dense particles even if they are larger in size. Although there were differences between export events in their intensity, the general pattern of marine snow community composition, sinking and attenuation during the first 5 events was the same (Supp. Fig. S6 and S7). Such consistency suggests their production by phytoplankton with a constant community composition unlike the Arctic bloom which showed a succession in primary producers types and marine snow morphotypes (Trudnowska et al., 2021). Contrasting with the first 5 export events, the last export event showed an increased contribution of agglomerates, possibly due to the coastal origin from the Congo river, or due to the most northern location with a different phytoplankton community composition or because aggregation mechanisms may have been different during this event (Sup. Fig. S3). The surface change in the community composition was mirrored in the mesopelagic layer probably resulting from sedimentation. However, sinking speeds, nor attenuation were different from the other events.

4.3 Sinking speed and vertical attenuation of different marine snow categories

Our sinking speed estimates for 500 µm - 1 mm size range particles (10-50 m d^{-1}) are in the same range as the few other estimates obtained with time series of export plume (Briggs et al., 2020; Lacour et al., 2024; Stemmann et al., 2002; Trudnowska et al., 2021) or obtained with *in situ* devices (Diercks and Asper, 1997; Iversen and Lampitt, 2020; Jouandet et al., 2011; Nowald et al., 2009). However, we calculate smaller sinking

speeds relative to other *ex-situ* estimates compiled in previous synthesis as illustrated by the difference between our estimates and the hierarchical regression in the data compilation of (Cael et al., 2021) (Fig. 8). Our sinking estimates are in good agreement with the previous model (Kriest, 2002) which was developed for miscellaneous aggregates. Thus our results confirm that sinking speeds of natural assemblage of marine snow differ from *ex situ* estimates, suggesting that the composition of the particles used in the experiments is biased toward fast sinking particles (Williams and Giering, 2022).

Not surprisingly, dense (darker appearances implying denser and more compact structures) marine snow particles (>500 µm) have faster sinking speed than more porous one, a property measured and modeled from experimental works (Giering et al., 2020) but never reported for *in situ* measurement in export plume. The sinking-to-size positive relationship was less obvious for a given aggregate morphotype because of their limited size range. The full size range was covered only for flakes whose sinking speed remained constant with size. However, strings and spheres had increasing sinking speeds with their size. Taken together, these two results confirm that the sinking speed to size relationship may exist for certain types of particles but is not universal (Iversen and Lampitt, 2020; Williams and Giering, 2022) as other morphological factors (here density) are at play. Among the different factors (phyto- and zoo- plankton community composition, inorganic ballasting) leading to denser particles (Francois et al., 2002; Guidi et al., 2016; Trudnowska et al., 2021; Turner, 2015), our study indicates phytoplankton aggregates to be principally responsible of the observed stronger export. Extending the size range to 100 µm and pooling all particles together confirms the size-to-sinking relationship with however strong variability between export plumes for the small particles and a limited size range up to the size class 1.0-1.63 mm. For the larger size range, sinking can only be estimated after classification because non-sinking aggregates (flakes and fibers) are dominant at the surface blurring the time series of all particles.

Carbon fluxes and their vertical attenuation for the different morphotypes was not calculated because the four categories did not match the few available sizes to POC conversion factors (Alldredge, 1998; Durkin et al., 2021). Instead, export efficiency was addressed from the vertical attenuation of the concentration of the four different categories in the plume. Abundance attenuation for the four morphotypes in the plume did not increase on average with particle size and showed that attenuation varied more with morphotypes than size. For a given size class (1.02-1.29 mm), dense morphotypes (agglomerates and spheres) had the lowest attenuation suggesting more efficient transfer to the deep ocean. The exponent cannot be directly compared to the literature because of the units but also because previous flux attenuation exponent were calculated in a vertical frame in which depth layers are temporarily disconnected (ie, at the time of sampling the surface layer is decoupled from the deep layers) while here we consider the number of particles in the sinking plume as they are consumed by different mesopelagic processes (Giering et al., 2014; Stemmann et al., 2004). We believe that following export plumes provide a more accurate estimation of the attenuation than calculating it from vertical profiles as usually done.

Apart from events 4 and 5, we believe that particle spatial gradients in the mesopelagic were low and that the large variability in the sinking speed estimates arise from other methodological factors that are important to discuss to improve further studies. First, the quality of the sinking estimates depend on the abundance of particles *in situ*. Compared to conditions with massive seasonal blooms over a long period of several months (Lacour et al., 2024), the production and export events in the Angola basin were less than 1.5 months with on average 10 times lower concentrations. Both factors yielded a patchy spatial distribution that was smoothed by using a depth bin of 100 m instead of varying depth bin (20 to 200 m) (Lacour et al., 2024). This high variability was amplified as large particles were subdivided in four morphotypes. Second, the deployment in the Angola basin took place close to coastal upwelling systems. Offshore propagating filaments may have had effects on particle vertical distribution mainly on small particles (here Bbp POC and MiP). Third, the clustering method is not sufficiently selective to obtain homogeneous groups among the aggregates as the overlaps can be seen on the PCA space (Supp. Fig. S1). This non-perfect classification has the effect of smoothing the derived estimates of sinking speed and attenuation.

5 Conclusion

We describe seven bloom events leading to surface accumulation of marine snow based on data obtained from a UVP6 camera mounted on a BGC-Argo float and recovered after one year of deployment. Six of them led to an export event with different types of aggregates and different penetration depths. For the first time, two core parameters for carbon sequestration, sinking speeds, and vertical attenuation, were calculated *in situ* for different sizes and morphotypes. Not all detected marine snow aggregates are sinking despite them being larger than 1 mm. Within a given size range, we show that sinking speeds of porous marine snow are smaller than that of dense marine snow indicating the strong impact of density on sinking speed. However, we show that size is still an important property to determine the sinking speed when considering a larger size range or a specific type of marine snow. Compared to earlier studies which could not distinguish aggregates morphology, the proposed classification allowed us to calculate sinking speeds of millimetric marine snow categories even in the case when the largest fraction marine snow are not sinking. Compared to published synthesis on marine particles sinking speeds, our *in situ* estimates are consistent with empirical allometric models parameterized for marine aggregates and lower than most *ex situ* estimates posing the question of the impact of the methodology. This study demonstrates the high potential of using cameras on autonomous floats to monitor planktonic ecosystems and assess intermittent export following episodic bloom events or induced by marine Carbon Dioxide Removal during large scale operations. To better understand particle dynamics and better assess carbon flux, future works should improve the following key methodological issues, 1) a global library of marine snow images to develop classification algorithm adapted for regional and global applications, 2) size to POC conversion factor for the different types of aggregates, 3) couple BGC-Argo floats with ship surveys to provide more comprehensive contextual data than only those derived from the float and satellite data as in this study, 4) increase acquisition frequency to detect rare larger particles, 5) implement embedded recognition of plankton and embedded classification of marine snow in camera because most of the floats are not recovered.

Author Contribution Statement

YDS, LS, RK, designed the study
YDS, MB, JH, AB, RL, LS, AA, PB, LD worked on the different components of the data analysis
AB calculated the Lagrangian metrics
YDS and LS drafted the manuscript
All authors reviewed the manuscript.

Competing interests

The contact author has declared that none of the authors has any competing interests

Acknowledgment

The authors acknowledge the support of the crew of RV Sonne during cruise SO283 and RV Meteor during cruise M181 for the deployment and recovery of the BGC-Argo float. We are thankful to Marc Picheral and Camille Catalano and the Plateforme d'Imagerie Quantitative de Villefranche (PIQv) to make the UVP6 data available. Argo data were collected and made freely available by the International Argo Program and the national programs that contribute to it. (https://argo.ucsd.edu, https://www.ocean-ops.org). The Argo Program is part of the Global Ocean Observing System. Argo float data and metadata from Global Data Assembly Centre (Argo GDAC). SEANOE. http://doi.org/10.17882/42182. RK acknowledges funding from the Heisenberg Programme of the German Science Foundation #KI 1387/5-1. RK and AB acknowledge support via a "Make Our Planet Great Again" grant of the French National Research Agency within the "Programme d'Investissements d'Avenir"; reference "ANR-19-MPGA-0012". AB, RK, LS, SSp, LD, PB acknowledge support via EU H2020 grant (agreement 817578 TRIATLAS project). AB acknowledges support via "SEASONS" project of the French National Center of Spatial Studies (CNES). LD acknowledges support via Sorbonne Université through the Ecole doctorale 129.

614 YDS acknowledges support via "Make Our Planet Great Again" visiting fellowship program for early career
615 researchers and granted by the French Ministry for Europe and Foreign Affairs, in collaboration with the French
616 Ministry for Higher Education and Research, and implemented by Campus France.
617
618

Bibliography

620 Accardo, A., Laxenaire, R., Baudena, A., Speich, S., Kiko, R., and Stemmann, L.: Massive and localized export
621 of selected marine snow types at eddy edges in the South Atlantic Ocean, EGUsphere, 2024, 1–29, 2024.
622 Aguedjou, H., Dadou, I., Chaigneau, A., Morel, Y., and Alory, G.: Eddies in the Tropical Atlantic Ocean and
623 their seasonal variability, Geophysical Research Letters, 46, 12156–12164, 2019.
624 Alldredge, A.: The carbon, nitrogen and mass content of marine snow as a function of aggregate size, Deep-Sea
625 Research Part I-Oceanographic Research Papers, 45, 529–541, 1998.
626 Alldredge, A. L. and Gotschalk, C.: In situ settling behavior of marine snow, Limnology and Oceanography, 33,
627 339–351, 1988.
628 Alldredge, A. L. and Silver, M. W.: Characteristics, dynamics and significance of marine snow, Prog.
629 Oceanogr., 20, 41–82, 1988.
630 Awo, F. M., Rouault, M., Ostrowski, M., Tomety, F. S., Da-Allada, C. Y., and Jouanno, J.: Seasonal cycle of
631 sea surface salinity in the Angola Upwelling System, Journal of Geophysical Research: Oceans, 127,
632 e2022JC018518, 2022.
633 Baudena, A., Ser-Giacomi, E., D'Onofrio, D., Capet, X., Cotté, C., Cherel, Y., and D'Ovidio, F.: Fine-scale
634 structures as spots of increased fish concentration in the open ocean. Sci Rep 11: 15805, 2021.
635 Biard, T., Stemmann, L., Picheral, M., Mayot, N., Vandromme, P., Hauss, H., Gorsky, G., Guidi, L., Kiko, R.,
636 and Not, F.: In situ imaging reveals the biomass of giant protists in the global ocean, Nature, 532, 504-+,
637 https://doi.org/10.1038/nature17652, 2016.
638 Boyd, P. W., Claustre, H., Levy, M., Siegel, D. A., and Weber, T.: Multi-faceted particle pumps drive carbon
639 sequestration in the ocean, Nature, 568, 327–335, 2019.
640 Brandt, P., Alory, G., Awo, F. M., Dengler, M., Djakouré, S., Imbol Koungue, R. A., Jouanno, J., Körner, M.,
641 Roch, M., and Rouault, M.: Physical processes and biological productivity in the upwelling regions of the
642 tropical Atlantic, Ocean Science, 19, 581–601, 2023.
643 Briggs, N., Dall'Olmo, G., and Claustre, H.: Major role of particle fragmentation in regulating biological
644 sequestration of CO2 by the oceans, Science, 367, 791-+, https://doi.org/10.1126/science.aay1790, 2020.
645 Burd, A. B.: Modeling the Vertical Flux of Organic Carbon in the Global Ocean, Annual review of marine
646 science, 16, 2023.
647 Burd, A. B., Hansell, D. A., Steinberg, D. K., Anderson, T. R., Aristegui, J., Baltar, F., Beaupre, S. R.,
648 Buesseler, K. O., DeHairs, F., Jackson, G. A., Kadko, D. C., Koppelmann, R., Lampitt, R. S., Nagata, T.,
649 Reinthaler, T., Robinson, C., Robison, B. H., Tamburini, C., and Tanaka, T.: Assessing the apparent imbalance
650 between geochemical and biochemical indicators of meso- and bathypelagic biological activity: What the @$#!
651 is wrong with present calculations of carbon budgets?, Deep-Sea Research Part Ii-Topical Studies in
652 Oceanography, 57, 1557–1571, https://doi.org/10.1016/j.dsr2.2010.02.022, 2010.
653 Cael, B., Cavan, E. L., and Britten, G. L.: Reconciling the size-dependence of marine particle sinking speed,
654 Geophysical Research Letters, 48, e2020GL091771, 2021.
655 Chambault, P., Baudena, A., Bjorndal, K. A., Santos, M. A., Bolten, A. B., and Vandeperre, F.: Swirling in the
656 ocean: Immature loggerhead turtles seasonally target old anticyclonic eddies at the fringe of the North Atlantic
657 gyre, Progress in Oceanography, 175, 345–358, 2019.
658 Checkley, D. M., Davis, R. E., Herman, A. W., Jackson, G. A., Beanlands, B., and Regier, L. A.: Assessing
659 plankton and other particles in situ with the SOLOPC, Limnology and Oceanography, 53, 2123–2136, 2008.
660 Diercks, A. R. and Asper, V. L.: In situ settling speeds of marine snow aggregates below the mixed layer: Black
661 Sea and Gulf of Mexico, Deep-Sea Research Part I-Oceanographic Research Papers, 44, 385–398, 1997.
662 Drago, L., Panaiotis, T., Irisson, J.-O., Babin, M., Biard, T., Carlotti, F., Coppola, L., Guidi, L., Hauss, H.,
663 Karp-Boss, L., Lombard, F., McDonnell, A. M. P., Picheral, M., Rogge, A., Waite, A. M., Stemmann, L., and
664 Kiko, R.: Global Distribution of Zooplankton Biomass Estimated by In Situ Imaging and Machine Learning,
665 FRONTIERS IN MARINE SCIENCE, 9, https://doi.org/10.3389/fmars.2022.894372, 2022.
666 Durkin, C. A., Buesseler, K. O., Cetinić, I., Estapa, M. L., Kelly, R. P., and Omand, M.: A visual tour of carbon
667 export by sinking particles, Global Biogeochemical Cycles, 35, e2021GB006985, 2021.
668 Durrieu de Madron, X., Nyffeler, F., and Godet, C. H.: Hydrographic structure and nepheloid spatial distribution
669 in the Gulf of Lions continental margin, Continental Shelf Research, 10, 915–929, 1990.
670 Durrieu de Madron, X., Ramondenc, S., Berline, L., Houpert, L., Bosse, A., Martini, S., Guidi, L., Conan, P.,

671   Curtil, C., and Delsaut, N.: Deep sediment resuspension and thick nepheloid layer generation by open-ocean
672   convection, Journal of Geophysical Research: Oceans, 122, 2291–2318, 2017.
673   Forest, A., Stemmann, L., Picheral, M., Burdorf, L., Robert, D., Fortier, L., and Babin, M.: Size distribution of
674   particles and zooplankton across the shelf-basin system in southeast Beaufort Sea: combined results from an
675   Underwater Vision Profiler and vertical net tows, Biogeosciences, 9, 1301–1320, https://doi.org/Doi
676   10.5194/Bg-9-1301-2012, 2012.
677   Forest, A., Babin, M., Stemmann, L., Picheral, M., Sampei, M., Fortier, L., Gratton, Y., Belanger, S., Devred,
678   E., Sahlin, J., Doxaran, D., Joux, F., Ortega-Retuerta, E., Martin, J., Jeffrey, W. H., Gasser, B., and Miquel, J.
679   C.: Ecosystem function and particle flux dynamics across the Mackenzie Shelf (Beaufort Sea, Arctic Ocean): an
680   integrative analysis of spatial variability and biophysical forcings, Biogeosciences, 10, 2833–2866,
681   https://doi.org/10.5194/bg-10-2833-2013, 2013.
682   Francois, R., Honjo, S., Krishfield, R., and Manganini, S.: Factors controlling the flux of organic carbon to the
683   bathypelagic zone of the ocean, Global Biogeochem. Cycles, 16, [doi:10.1029/2001GB001722], 2002.
684   Giering, S. L. C., Richard Sanders, Richard S. Lampitt, Thomas R. Anderson, Christian Tamburini, Mehdi
685   Boutrif, Mikhail V. Zubkov, Chris M. Marsay, Stephanie A. Henson, Kevin Saw, Kathryn Cook, and Daniel J.
686   Mayor: Reconciliation of the carbon budget in the ocean's twilight zone, Nature, 507, 17,
687   https://doi.org/10.1038/nature13123, 2014.
688   Giering, S. L. C., Cavan, E. L., Basedow, S. L., Briggs, N., Burd, A. B., Darroch, L. J., Guidi, L., Irisson, J. O.,
689   Iversen, M. H., Kiko, R., Lindsay, D., Marcolin, C. R., McDonnell, A. M. P., Moller, K. O., Passow, U.,
690   Thomalla, S., Trull, T. W., and Waite, A. M.: Sinking Organic Particles in the Ocean-Flux Estimates From in
691   situ Optical Devices, Frontiers in Marine Science, 6, https://doi.org/10.3389/fmars.2019.00834, 2020.
692   Gonzalez-Quiros, R. and Checkley, D. M.: Occurrence of fragile particles inferred from optical plankton
693   counters used in situ and to analyze net samples collected simultaneously, Journal of Geophysical Research-
694   Oceans, 111, 2006.
695   Gorsky, G., Picheral, M., and Stemmann, L.: Use of the Underwater Video Profiler for the study of aggregate
696   dynamics in the North Mediterranean, Estuarine Coastal and Shelf Science, 50, 121–128, 2000.
697   Guidi, L., Jackson, G. A., Stemmann, L., Miquel, J. C., Picheral, M., and Gorsky, G.: Relationship between
698   particle size distribution and flux in the mesopelagic zone, Deep Sea Research Part I: Oceanographic Research
699   Papers, 55, 1364–1374, https://doi.org/10.1016/j.dsr.2008.05.014, 2008.
700   Guidi, L., Legendre, L., Reygondeau, G., Uitz, J., Stemmann, L., and Henson, S. A.: A new look at ocean
701   carbon remineralization for estimating deepwater sequestration, Global Biogeochem. Cycles, 29, 1044–1059,
702   https://doi.org/10.1002/2014gb005063, 2015.
703   Guidi, L., Chaffron, S., Bittner, L., Eveillard, D., Larhlimi, A., Roux, S., Darzi, Y., Audic, S., Berline, L., Brum,
704   J. R., Coelho, L. P., Espinoza, J. C. I., Malviya, S., Sunagawa, S., Dimier, C., Kandels-Lewis, S., Picheral, M.,
705   Poulain, J., Searson, S., Stemmann, L., Not, F., Hingamp, P., Speich, S., Follows, M., Karp-Boss, L., Boss, E.,
706   Ogata, H., Pesant, S., Weissenbach, J., Wincker, P., Acinas, S. G., Bork, P., de Vargas, C., Iudicone, D.,
707   Sullivan, M. B., Raes, J., Karsenti, E., Bowler, C., Gorsky, G., and Tara Oceans Consortium Coordinator:
708   Plankton networks driving carbon export in the oligotrophic ocean, Nature, 532, 465-+, 2016.
709   Henson, S., Bisson, K., Hammond, M., Martin, A., Mouw, C., and Yool, A.: Effect of sampling bias on global
710   estimates of ocean carbon export, Environmental Research Letters, 2024.
711   Honjo, S., Manganini, S. J., and Cole, J. J.: Sedimentation of biogenic matter in the deep ocean, Deep-Sea
712   Research, 29, 609–625, 1982.
713   Imbol Koungue, R. A., Brandt, P., Prigent, A., Aroucha, L. C., Lübbecke, J., Imbol Nkwinkwa, A. S. N.,
714   Dengler, M., and Keenlyside, N.: Drivers and impact of the 2021 extreme warm event in the tropical Angolan
715   upwelling system, Scientific Reports, 14, 16824, 2024.
716   Irisson, J.-O., Ayata, S.-D., Lindsay, D. J., Karp-Boss, L., and Stemmann, L.: Machine Learning for the Study
717   of Plankton and Marine Snow from Images., Annual review of marine science, 14, 277–301,
718   https://doi.org/10.1146/annurev-marine-041921-013023, 2022.
719   Iversen, M. H. and Lampitt, R. S.: Size does not matter after all: no evidence for a size-sinking relationship for
720   marine snow, Progress in Oceanography, 189, 102445, 2020.
721   Iversen, M. H., Nowald, N., Ploug, H., Jackson, G. A., and Fischer, G.: High resolution profiles of vertical
722   particulate organic matter export off Cape Blanc, Mauritania: Degradation processes and ballasting effects,
723   Deep-Sea Research Part I-Oceanographic Research Papers, 57, 771–784,
724   https://doi.org/10.1016/j.dsr.2010.03.007, 2010.
725   Jackson, G. A. and Checkley, D. M.: Particle size distributions in the upper 100 m water column and their
726   implications for animal feeding in the plankton, Deep-Sea Research Part I-Oceanographic Research Papers, 58,
727   283–297, https://doi.org/10.1016/j.dsr.2010.12.008, 2011.
728   Jouandet, M.-P., Trull, T. W., Guidi, L., Picheral, M., Ebersbach, F., Stemmann, L., and Blain, S.: Optical
729   imaging of mesopelagic particles indicates deep carbon flux beneath a natural iron-fertilized bloom in the
730   Southern Ocean, Limnology and Oceanography, 56, 1130–1140, https://doi.org/10.4319/lo.2011.56.3.1130,

2011.

Kiko, R., Biastoch, A., Brandt, P., Cravatte, S., Hauss, H., Hummels, R., Kriest, I., Marin, F., McDonnell, A. M. P., Oschlies, A., Picheral, M., Schwarzkopf, F. U., Thurnherr, A. M., and Stemmann, L.: Biological and physical influences on marine snowfall at the equator, Nature Geoscience, 10, 852-+, https://doi.org/10.1038/ngeo3042, 2017.

Kiko, R., Brandt, P., Christiansen, S., Faustmann, J., Kriest, I., Rodrigues, E., Schütte, F., and Hauss, H.: Zooplankton-mediated fluxes in the eastern tropical North Atlantic, Frontiers in Marine Science, 7, 358, 2020.

Kopte, R., Brandt, P., Dengler, M., Tchipalanga, P., Macuéria, M., and Ostrowski, M.: The A ngola C urrent: Flow and hydrographic characteristics as observed at 11° S, Journal of Geophysical Research: Oceans, 122, 1177–1189, 2017.

Körner, M., Brandt, P., and Dengler, M.: Seasonal cycle of sea surface temperature in the tropical Angolan Upwelling System, Ocean Science, 19, 121–139, 2023.

Körner, M., Brandt, P., Illig, S., Dengler, M., Subramaniam, A., Bachèlery, M.-L., and Krahmann, G.: Coastal trapped waves and tidal mixing control primary production in the tropical Angolan upwelling system, Science Advances, 10, eadj6686, 2024.

Kriest, I.: Different parameterizations of marine snow in a 1D-model and their influence on representation of marine snow, nitrogen budget and sedimentation, Deep Sea Research Part I: Oceanographic Research Papers, 49, 2133–2162, 2002.

Kriest, I. and Evans, G. T.: A vertically resolved model for phytoplankton aggregation, Proceedings of the Indian Academy of Sciences-Earth & Planetary Sciences, 109, 453–469, 2000.

Lacour, L., Briggs, N., Petiteau, L., Bressac, M., Guidi, L., Castro, B. F., Picheral, M., Catalano, C., Schmechtig, C., and Leymarie, E.: Particle size sets the carbon penetration depth during ocean bloom export events, 2024.

Laget, M., Drago, L., Panaïotis, T., Kiko, R., Stemmann, L., Rogge, A., Llopis-Monferrer, N., Leynaert, A., Irisson, J.-O., and Biard, T.: Global census of the significance of giant mesopelagic protists to the marine carbon and silicon cycles, Nature Communications, 15, 3341, 2024.

Laurenceau-Cornec, E. C., Trull, T. W., Davies, D. M., Christina, L., and Blain, S.: Phytoplankton morphology controls on marine snow sinking velocity, Marine Ecology Progress Series, 520, 35–56, 2015.

Legendre, P. and Legendre, L.: Chapter 11 - Canonical analysis, in: Developments in Environmental Modelling, vol. 24, edited by: Legendre, P. and Legendre, L., Elsevier, 625–710, https://doi.org/10.1016/B978-0-444-53868-0.50011-3, 2012.

Martin, J. H., Knauer, G. A., Karl, D. M., and Broenkow, W. W.: VERTEX: carbon cycling in the northeast Pacific, Deep Sea Research Part A. Oceanographic Research Papers, 34, 267–285, 1987.

McDonnell, A. M. P. and Buesseler, K. O.: Variability in the average sinking velocity of marine particles, Limnology and Oceanography, 55, 2085–2096, https://doi.org/10.4319/lo.2010.55.5.2085, 2010.

McInnes, L., Healy, J., and Melville, J.: Umap: Uniform manifold approximation and projection for dimension reduction, arXiv preprint arXiv:1802.03426, 2018.

Nowald, N., Fischer, G., Ratmeyer, V., Iversen, M., Reuter, C., Wefer, G., and Ieee: In-situ sinking speed measurements of marine snow aggregates acquired with a settling chamber mounted to the Cherokee ROV, in: Oceans 2009 - Europe, Vols 1 and 2, 1286–1291, 2009.

Panaiotis, T., Babin, M., Biard, T., Carlotti, F., Coppola, L., Guidi, L., Hauss, H., Karp-Boss, L., Kiko, R., Lombard, F., McDonnell, A. M. P., Picheral, M., Rogge, A., Waite, A. M., Stemmann, L., and Irisson, J.-O.: Three major mesoplanktonic communities resolved by in situ imaging in the upper 500 m of the global ocean, GLOBAL ECOLOGY AND BIOGEOGRAPHY, https://doi.org/10.1111/geb.13741, 2023.

Picheral, M., Guidi, L., Stemmann, L., Karl, D. M., Iddaoud, G., and Gorsky, G.: The Underwater Vision Profiler 5: An advanced instrument for high spatial resolution studies of particle size spectra and zooplankton, Limnology and Oceanography-Methods, 8, 462–473, https://doi.org/10.4319/lom.2010.8.462, 2010.

Picheral, M., Catalano, C., Brousseau, D., Claustre, H., Coppola, L., Leymarie, E., Coindat, J., Dias, F., Fevre, S., Guidi, L., Irisson, J. O., Legendre, L., Lombard, F., Mortier, L., Penkerch, C., Rogge, A., Schmechtig, C., Thibault, S., Tixier, T., Waite, A., and Stemmann, L.: The Underwater Vision Profiler 6: an imaging sensor of particle size spectra and plankton, for autonomous and cabled platforms, LIMNOLOGY AND OCEANOGRAPHY-METHODS, 20, 115–129, https://doi.org/10.1002/lom3.10475, 2022.

Ploug, H., Iversen, M. H., and Fischer, G.: Ballast, sinking velocity, and apparent diffusivity within marine snow and zooplankton fecal pellets: Implications for substrate turnover by attached bacteria, Limnology and Oceanography, 53, 1878–1886, 2008a.

Ploug, H., Iversen, M. H., Koski, M., and Buitenhuis, E. T.: Production, oxygen respiration rates, and sinking velocity of copepod fecal pellets: Direct measurements of ballasting by opal and calcite, Limnology and Oceanography, 53, 469–476, 2008b.

Ploug, H., Terbruggen, A., Kaufmann, A., Wolf-Gladrow, D., and Passow, U.: A novel method to measure particle sinking velocity in vitro, and its comparison to three other in vitro methods, Limnology and

791   Oceanography-Methods, 8, 386–393, https://doi.org/10.4319/lom.2010.8.386, 2010.
792   Scannell, H. A. and McPhaden, M. J.: Seasonal mixed layer temperature balance in the southeastern tropical
793   Atlantic, Journal of Geophysical Research: Oceans, 123, 5557–5570, 2018.
794   Ser-Giacomi, E., Baudena, A., Rossi, V., Follows, M., Clayton, S., Vasile, R., López, C., and Hernández-García,
795   E.: Lagrangian betweenness as a measure of bottlenecks in dynamical systems with oceanographic examples,
796   Nature communications, 12, 4935, 2021.
797   Shadden, S. C., Lekien, F., and Marsden, J. E.: Definition and properties of Lagrangian coherent structures from
798   finite-time Lyapunov exponents in two-dimensional aperiodic flows, Physica D: Nonlinear Phenomena, 212,
799   271–304, 2005.
800   Siegel, D. A., DeVries, T., Cetinić, I., and Bisson, K. M.: Quantifying the Ocean's Biological Pump and Its
801   Carbon Cycle Impacts on Global Scales, Annual review of marine science, 15, 329–356, 2023.
802   Soviadan, Y. D., Benedetti, F., Brandão, M. C., Ayata, S.-D., Irisson, J.-O., Jamet, J. L., Kiko, R., Lombard, F.,
803   Gnandi, K., and Stemmann, L.: Patterns of mesozooplankton community composition and vertical fluxes in the
804   global ocean, Progress in Oceanography, 200, 102717, https://doi.org/10.1016/j.pocean.2021.102717, 2022.
805   Stemmann, L. and Boss, E.: Plankton and Particle Size and Packaging: From Determining Optical Properties to
806   Driving the Biological Pump, Annu Rev Mar Sci, 4, 263–290, https://doi.org/Doi 10.1146/Annurev-Marine-
807   120710-100853, 2012.
808   Stemmann, L., Gorsky, G., Marty, J. C., Picheral, M., and Miquel, J. C.: Four-year study of large-particle
809   vertical distribution (0-1000 m) in the NW Mediterranean in relation to hydrology, phytoplankton, and vertical
810   flux, Deep-Sea Research Part Ii-Topical Studies in Oceanography, 49, 2143–2162, 2002.
811   Stemmann, L., Jackson, G. A., and Gorsky, G.: A vertical model of particle size distributions and fluxes in the
812   midwater column that includes biological and physical processes - Part II: application to a three year survey in
813   the NW Mediterranean Sea, Deep-Sea Research Part I-Oceanographic Research Papers, 51, 885–908,
814   https://doi.org/10.1016/j.dsr.2004.03.002, 2004.
815   Stemmann, L., Youngbluth, M., Robert, K., Hosia, A., Picheral, M., Paterson, H., Ibanez, F., Guidi, L.,
816   Lombard, F., and Gorsky, G.: Global zoogeography of fragile macrozooplankton in the upper 100-1000 m
817   inferred from the underwater video profiler, Ices Journal of Marine Science, 65, 433–442,
818   https://doi.org/10.1093/icesjms/fsn010, 2008.
819   Stolarek, I., Samelak-Czajka, A., Figlerowicz, M., and Jackowiak, P.: Dimensionality reduction by UMAP for
820   visualizing and aiding in classification of imaging flow cytometry data, iScience, 25, 105142,
821   https://doi.org/10.1016/j.isci.2022.105142, 2022.
822   Teixeira, J., Rocha, V., Oliveira, J., Jorge, P. A. S., and Silva, N. A.: Towards real-time identification of trapped
823   particles with UMAP-based classifiers, J. Phys.: Conf. Ser., 2407, 012043, https://doi.org/10.1088/1742-
824   6596/2407/1/012043, 2022.
825   Trudnowska, E., Lacour, L., Ardyna, M., Rogge, A., Irisson, J. O., Waite, A. M., Babin, M., and Stemmann, L.:
826   Marine snow morphology illuminates the evolution of phytoplankton blooms and determines their subsequent
827   vertical export., Nature communications, 12, 2816–2816, https://doi.org/10.1038/s41467-021-22994-4, 2021.
828   Turner, J. T.: Zooplankton fecal pellets, marine snow, phytodetritus and the ocean's biological pump, Progress
829   in Oceanography, 130, 205–248, 2015.
830   Volk, T. and Hoffert, M. I.: Ocean carbon pumps: analysis of relative strengths and efficiencies in ocean-driven
831   atmospheric CO2 changes, in: The Carbon Cycle and Atmospheric CO2: Natural Variations Archean to Present,
832   vol. 32, edited by: Sundquist, E. T. and Broecker, W. S., Washington, D.C, 99–110, 1985.
833   Williams, J. and Giering, S.: In situ particle measurements deemphasize the role of size in governing the sinking
834   velocity of marine particles, Geophysical Research Letters, 49, e2022GL099563, 2022.
835   Yeo, I. and Johnson, R. A.: A new family of power transformations to improve normality or symmetry,
836   Biometrika, 87, 954–959, https://doi.org/10.1093/biomet/87.4.954, 2000.